FROM THE DEPARTMENT OF RADIOLOGY, UNIVERSITY OF COLORADO MEDICAL CENTER, DENVER, COLORADO 80220, USA.

CROSS-SECTIONAL ANATOMIC IMAGES BY GAMMA RAY TRANSMISSION SCANNING

G. A. THIEME, W. R. HENDEE, G. S. IBBOTT, P. L. CARSON and D. L. KIRCH

In the present practice of radiation therapy, a treatment regimen for a patient usually is selected by examining dose distributions computed for one or more treatment plans proposed for the patient. Rarely are the dose distributions corrected for perturbations introduced by inhomogeneous structures such as lung and bone between the beam entrance surfaces and the treated region. These perturbations are not accounted for, even though they may affect the tumor dose by as much as 20 to 30 percent, primarily because the exact location and extent of the inhomogeneous regions within the patient are unknown.

Various techniques have been proposed for delineation of the cross-sectional anatomy of patients scheduled for radiation therapy. Among the techniques are:

(1) demonstration of cross-sectional anatomic displays from orthogonal roentgenograms projected in a special viewing device. This approach suffers from inaccuracy, the need for a special viewing device, the time required to align the roentgenograms, the corrections necessary for differences in magnification of the roentgenograms, and, most important, the inflexible positioning requirements for film exposure which are difficult to satisfy with seriously ill patients;

(2) display of cross-sectional anatomy on roentgenograms obtained by transverse

Submitted for publication 5 March 1974.

tomography. The cost of transverse tomographic equipment capable of flexible patient positioning, and the poor quality of transverse tomographic images, are the major limitations of this technique;

(3) representation of cross-sectional anatomy by obtaining individual patient contours and superimposing standard anatomic displays available in pictoral atlases. This method is no more than a crude approximation, because it offers no compensation for anatomic variations among patients;

(4) development of cross-sectional anatomic displays by B-mode ultrasound scanning. This approach is being utilized in a few institutions, including our own. However, the usefulness of ultrasound scanning techniques in the thorax, the region where dose perturbations caused by inhomogeneities may be greatest, is limited severely by the poor transmission of ultrasound energy in lung. Furthermore, current B-mode ultrasound techniques provide only limited information about the internal anatomy of patients, primarily because the information contained in the amplitude of returning ultrasound pulses is discarded. Current work in ultrasound B-mode imaging, involving the development of constant depth scanning techniques, promises to improve the spatial resolution and amplitude information of ultrasound images. As this work has progressed, it has become clear that ultrasound imaging of internal anatomy is complementary to, and not competitive with, the approach to delineation of cross-sectional anatomy outlined in this report. Moreover, it has become apparent that ultrasound scanning at constant depth may be more amenable to tumor localization and, possibly, identification, than to display of cross-sectional anatomy across an entire plane containing a tumor;

(5) determination of cross-sectional anatomy by measurement of roentgen or γ-ray transmission through the patient at a number of angular orientations, and reconstruction of cross-sectional images by data processing techniques; this approach is described here.

Some attention already has been directed toward the demonstration of cross-sectional anatomy by roentgen or γ-ray scanning. CORMACK (1964, 1973) has examined the problem mathematically and experimentally in an effort to identify a method for outlining the cross-sectional anatomy of radiation therapy patients. However, both the experimental apparatus and the mathematical reconstruction process used by CORMACK were intentionally simplistic, because they were developed primarily as a test of the feasibility of the approach. Consequently, the question has remained unanswered of the practicality of roentgen or γ-ray transmission scanning for routine display of the cross-sectional anatomy of radiation therapy patients.

For many years, KUHL and his associates have been interested in the production of transverse tomographic images from data recorded by an isotope scanner which scans transversally across a patient containing an administered isotope (KUHL & EDWARDS 1970). Primarily, KUHL's work has been directed towards use of transverse tomographic scanning methods to improve the detectability of small concentrations of activity in the brain. Application of the analytic techniques developed by KUHL

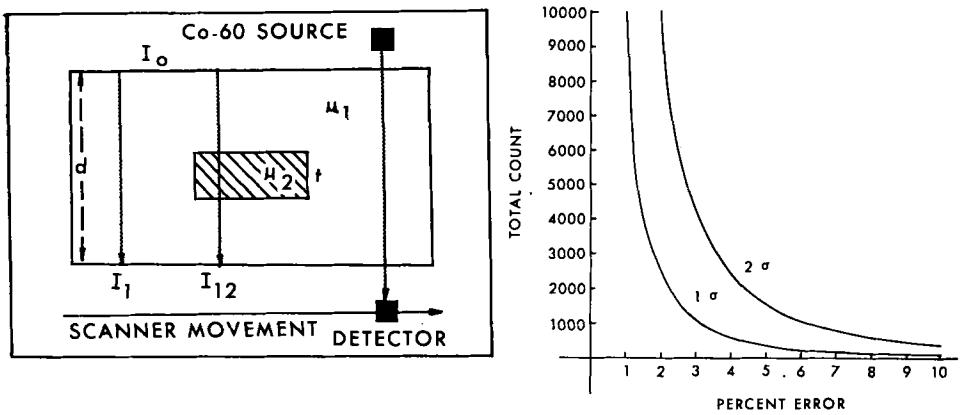

a b

Fig. 1. a) Muscle of thickness d (linear attenuation coefficient μ_1) containing an inhomogeneity (bone or lung tissue) of thickness t (linear attenuation coefficient μ_2). To obtain transmission data, the ^{60}Co source and detector move synchronously on opposite sides of the medium. b) Relationships among the significance and confidence levels and the minimum number N of detected photons.

to the transmission data collected in the present work produced reassembled images with unacceptably poor resolution and considerable distortion.

A few persons have attempted to use linear equations in the construction of three-dimensional images from two-dimensional projections (GORDON et coll. 1970, GOITIEN 1971, GILBERT 1972, SMITH et coll. 1973). This method appears impractical for the project described here, primarily because the number of linear equations is too formidable.

A potentially more useful approach is that described by RADON (1917). This work offers an approach to computation of surface integrals analogous to certain physical processes such as transmission γ-ray scanning at increments around a circle encompassing the patient. Limitations in RADON's approach, including its suitability primarily for objects of spherical shape with constant attenuation coefficients, have led to selection of an alternate approach for the project described here.

Recently, FARMER & COLLINS (1971) described an approach to delineation of anatomic cross sections which, in some ways, resembles the method described in this report. These investigators used a Ge(Li) detector and pulse height analyzer to detect scattered photons as a ^{137}Cs source was scanned across a phantom. Successive scans at different elevations were displayed on an oscilloscope screen to produce a two-dimensional image of the cross section of the phantom. No data processing, other than background cut off, was employed. For a patient thickness of 30 cm, the theoretical spatial resolution is quoted as 5 mm for the Farmer-Collins method. Limitations of this method include considerable variations in intensity and spatial resolution over the displayed image, particulary for patients of thickness greater

Table 1

Linear attenuation coefficients for muscle, compact bone, and lung, and fractional changes b in the transmission of 1.25 MeV γ-ray photon when lung or compact bone of thickness t is present in muscle

Material	Linear attenuation coefficient (cm^{-1}) 1.25 MeV photons	Thickness		
		t (cm)	b (bone)	b (lung)
Muscle	0.064*	0.25	+0.013	−0.011
Compact bone	0.114*	0.50	+0.025	−0.021
Lung	0.021**	1.00	+0.051	−0.042
		1.50	+0.078	−0.062
		2.00	+0.105	−0.082

* From JOHNS & CUNNINGHAM
** From IBBOTT & HENDEE

than 30 cm. As an alternative to the Farmer-Collins method, the method discussed below provides increased sensitivity by measurement of transmitted rather than scattered photons and by employment of a higher photon yield ^{60}Co source in place of ^{137}Cs.

Instrumentation design

Discussed in this section are physical considerations affecting the design and performance of a γ-ray transmission scanner. In Fig. 1 a, muscle of thickness d and linear attenuation coefficient μ_1 for photons of energy E surrounds an inhomogeneous structure such as lung or bone of thickness t and linear attenuation coefficient μ_2 for photons of the same energy. A narrow beam of monoenergetic γ-ray photons passes through the medium and impinges upon a detector equipped with a pinhole collimator. With proper collimation of the γ-ray beam and detector, the influence of scattered radiation can be minimized, and the fraction of γ-ray photons transmitted through the medium is an exponential function which varies only with the attenuation coefficients and the thicknesses of the materials traversed. That is,

$$I_1 = I_0 \, \mathrm{EXP}\,(-\mu_1 d) \tag{1}$$

where $\mathrm{EXP}\,(-\mu_1 d)$ is the fractional transmission of the γ-ray beam passing only through muscle, and

$$I_{12} = I_0 \, \mathrm{EXP}\,[-\mu_1(d-t)]\,\mathrm{EXP}\,(-\mu_2 t) \tag{2}$$

where $\mathrm{EXP}\,[-\mu_1(d-t)]\,\mathrm{EXP}\,(-\mu_2 t)$ is the fractional transmission of the γ-ray beam passing through both muscle and lung or bone.

If b is defined as the fractional change in beam intensity caused by the presence of an inhomogeneity of thickness t, then

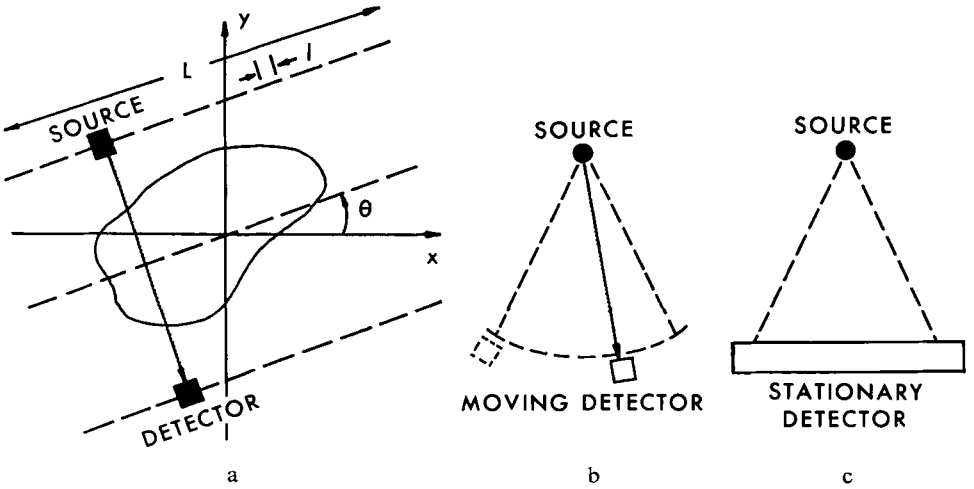

Fig. 2. Different approaches to γ-ray transmission scanning, including (a) moving source, moving detector technique, (b) stationary source, moving detector technique, and (c) stationary source, stationary detector technique.

$$b = \frac{I_1 - I_{12}}{I_1} = 1 - EXP\,[-(\mu_2 - \mu_1)\,t] \tag{3}$$

That is, the fractional change in beam intensity depends only upon the thickness of the inhomogeneity and the linear attenuation coefficients of the two materials. Linear attenuation coefficients for muscle, compact bone and lung irradiated with photons of 1.25 MeV, the average energy of γ-ray photons from ^{60}Co, are listed in Table 1. Included in the table are fractional changes in γ-ray transmission computed for different thicknesses of bone or lung embedded in muscle and irradiated with 1.25 MeV photons. Positive values of b indicate an inhomogeneity with a linear attenuation coefficient greater than that for muscle, and negative values imply an inhomogeneity with a coefficient smaller than that for muscle.

For a 0.25 cm thick inhomogeneity of either bone or lung in muscle, the change in beam intensity is slightly greater than 1 percent. Whether a measured change of 1 percent in beam intensity is considered statistically reliable, and indicative of a change in physical density along the beam path, depends upon the total number N of photons collected for the measurement and upon the confidence and significance levels chosen as statistical criteria (Fig. 1 b).

For gamma transmission measurements, ^{60}Co was chosen as the source of γ-ray photons. Advantages of ^{60}Co include: (1) high specific activity; (2) ready availability at reasonable cost; (3) decay to a stable product; (4) emission of two γ-ray photons, each with an emission probability >99 percent; (5) negligible error introduced by considering the emitted photons (1.17 and 1.33 MeV) as photons of a single average

energy of 1.25 MeV; (6) photon attenuation almost entirely by Compton interaction; and (7) high transmission of photons in biologic tissues.

Two approaches to transmission scanning, a moving source technique and a stationary source technique, were considered (Fig. 2). For the moving source approach, transmission data are obtained with a tightly collimated source and detector moving linearly and in synchrony on opposite sides of the patient at an angle θ with respect to a reference axis (Fig. 2 a). For the stationary point source technique, either a pencil beam of radiation is swept across the patient in synchrony with a single moving detector (Fig. 2 b), or a wedge of radiation is directed through the patient onto a long, stationary detector with adequate spatial resolution (Fig. 2 c). Analysis of the image reconstruction process for both approaches favors the parallel beam approach to transmission scanning. Consequently, this approach has been employed for the investigation described here.

If a scan interval (the distance between successive transmission measurements) is represented by I, and the total linear scan distance for one angular orientation of source and detector is represented by L, then the number of transmission measurements M per orientation is $M = L/I$.

With the fractional transmission through the maximum thickness of tissue encountered during the scan represented as P, and the total time required to scan a distance L designated as T, the measurement time at each of M points along L is T/M or TI/L. For the maximum tissue thickness encountered during the scan, at least N photons must be detected, where N is the minimum number of photons required for the desired level of statistical significance. This number of photons would increase to N/P in the absence of tissue. The number N/P of photons must be detected in the interval TI/L; consequently, the photon detection system must be capable of detecting photons at a rate δ equal to

$$\delta = \frac{N/P}{TI/L} = \frac{NL}{TIP} \tag{4}$$

The parameter δ is an important consideration in the selection of a photon detection system for γ-ray transmission scanning.

For detection of photons at the rate δ, the source must supply photons at a rate Φ equal to

$$\Phi = \frac{\delta}{\varepsilon A} = \frac{NL}{\varepsilon ATIP} \tag{5}$$

where Φ is the photon flux density at the detector, A is the cross-sectional area of the detector collimator, and ε is the detector efficiency. The photon flux density is related to the exposure rate χ by

$$\frac{\Phi}{X} = \frac{1.5 \times 10^3}{h\nu(\mu_{en})} \tag{6}$$

with Φ, χ, $h\nu$, and μ_{en} in units of photon/cm^2 – s, R/h, MeV, and m^2/kg in air, respectively. For ^{60}Co, $h\nu = 1.25$ MeV and $(\mu_{en}) = 2.67 \times 10^{-3}$ m^2/kg for air, and the exposure rate χ necessary for a photon flux density Φ is

$$\chi(\text{R/h}) = 2.23 \times 10^{-6}\, \Phi(\text{photon/cm}^2 - \text{s}) \tag{7}$$

A lower limit (self-absorption neglected) on the activity of a ^{60}Co source which will provide an exposure rate χ at a distance r in meters is

$$N_{Ci} = \frac{\chi(\text{R/h})\, r^2}{\Gamma} \tag{8}$$

where N_{Ci} is the activity in curies, and Γ is the exposure rate constant ($\Gamma = 1.29$ R/h – Ci at 1 meter for ^{60}Co). By combining equations (5), (7), and (8), the minimum ^{60}Co source activity required for a least N detected photons per measurement point may be written

$$N_{Ci} = \frac{2.23 \times 10^{-6} N L r^2}{\varepsilon A T I P \Gamma} \tag{9}$$

Equation (9) illustrates the importance of detector efficiency in minimizing source size and patient exposure to radiation, and suggests that a high efficiency scintillation detector is preferable to an ionization chamber for γ-ray transmission measurements. However, the choice of a detector also depends upon the ability of various detectors to respond to high photon flux densities. To estimate the maximum photon flux density to which a detector must respond, a maximum patient thickness of 40 cm (fractional transmission $P = 0.077$ for ^{60}Co photons in muscle) and a smallest scan interval I of 0.25 cm may be assumed. For any patient, the scan time should not exceed, say, 30 minutes. In actual practice, a scan time of < 5 minutes may be desired to reduce voluntary motion artefacts. If no deconvolution and data smoothing techniques are used during image reconstruction, 120 separate transmission scans would be required to satisfy the image reconstruction criterion described later. In a fully automated scanner, a time T of 10 seconds might be needed to scan a 40 cm length at a constant speed of 4 cm/s. If rotation of the source-detector assembly by 1.5° requires 3 seconds, then each transmission scan at a separate angular orientation would require 13 seconds, and 26 minutes would be required to accumulate transmission data for 120 orientations. For 1 percent, 1 σ counting statistics, at least 10 000 photons must be detected at each measurement point. With these values, a maximum photon detection rate δ of 2.08×10^6 photons/s is required (Eq. 4).

The computed photon detection rate is twice the maximum detection rate for a NaI detector operated in pulse mode (Table 2). Hence, use of a NaI detector in pulse mode appears marginal for transmission scanning.

To take advantage of the high detection efficiency of NaI for ^{60}Co photons, the detector may be operated in current mode, where limitations on the photon detec-

Table 2

Characteristics of common scintillators (in part from KAISER)

Scintillator	Time constant τ (μs)	Density (g/cm^3)	Detection efficiency relative to anthracene	Maximum detection rate for pulse mode operation (photon/s)
NaI(Tl)	0.25	3.67	2.1	8.7×10^5
CsI(Tl)	1.1	4.51	1.75	2.0×10^5
CsI(Na)	0.65	4.51	1.10	3.3×10^5
Anthracene	0.032	1.25	1.00	6.8×10^6
Plastics	0.0025–0.005	1.06	0.28–0.48	$4.3–8.7 \times 10^7$
Liquid	0.0015–0.008	0.86	0.27–0.49	$2.7–14.5 \times 10^7$

tion rate are imposed by the characteristics of the photomultiplier tube rather than NaI. Another advantage of current mode operation is an increase in detection efficiency for ^{60}Co photons. For example, a 4.5 cm diameter, 4 cm long NaI detector operated in pulse mode under conditions of photopeak counting yields a detection efficiency of 22 percent; in current mode, the detection efficiency is close to 61.5 percent (BERGER & DOGGET 1956). For a maximum patient thickness of 30 cm and a total scan time of up to 30 min, the source activity could be 60 percent less than that required for a 40 cm thick patient, and operation of a NaI detector in pulse mode would be marginally acceptable. With this source, however, more than 1 hour would be required to scan a 40 cm thick patient. However, operation of a NaI detector in current mode has two drawbacks. First, the signal is sensitive to slight changes in high voltage applied to the photomultiplier tube and signal amplification in the amplifier. Second, pulse height discrimination is not available to differentiate primary from scattered photons.

In our apparatus, signal drift is not noticeable provided that the amplifier and high voltage supply are turned on a few minutes before measurements are taken. To examine the handicap of using a NaI detector without pulse height discrimination, a ^{60}Co pulse height spectrum was measured with a 1×1 inch NaI detector. From the results, it was apparent that the lower discriminator of the pulse height analyzer must be set at about 1.05 MeV to include both photopeaks. This setting would transmit to the scaler pulses representing 1.33 MeV photons scattered through angles up to 26°, and 1.17 MeV photons scattered through angles up to 18°. That is, for a source-detector collimator arrangement with a scatter acceptance angle less than 18°, and negligible penetration of scattered photons through the collimator walls, pulse height analysis does not contribute to rejection of scattered photons when the lower level discriminator is set below both photopeaks. Consequently, the loss of pulse height analysis accompanying use of a NaI detector in current mode

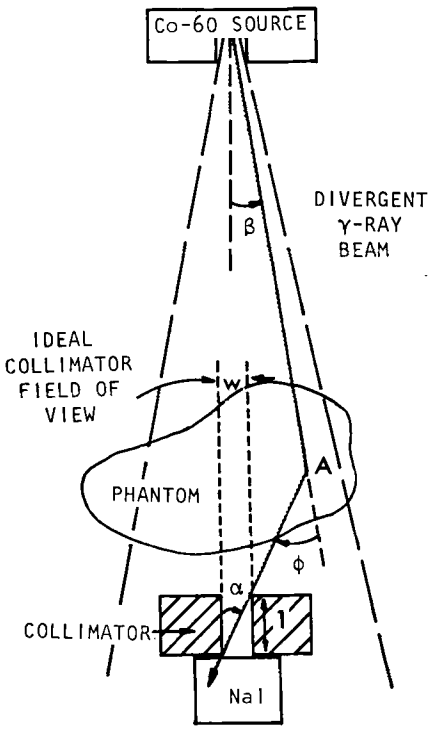

Fig. 3. Geometry for rejection of scattered photons by the detector collimator.

poses no handicap if the collimation of source and detector is made sufficiently restrictive.

The admission into a detector of photons scattered from outside the region of interest is illustrated in Fig. 3. With a detector collimator of length 1 and diameter w, the acceptance angle α for scattered photons entering the detector is $\alpha = \tan^{-1} w/l$. For a photon traversing the patient at an angle β with respect to the central axis of the collimator bore, the scattering angle Φ which will just permit a scattered photon to reach the detector is $\Phi = \alpha + \beta$. The amount of scattered radiation reaching the detector can be minimized by: (1) reducing α by decreasing the bore size w and increasing the length 1 of the detector collimator; and (2) reducing β by decreasing the diameter and increasing the length of the source collimator, at least to the limit of retaining a uniform photon flux density across the detector. Both of these options have been exercised in this investigation: the detector collimator slit has been reduced to dimensions comparable to the spatial resolution desired in the image, and the source collimator has been designed to provide a γ-ray beam which only slightly overlaps the detector collimator slit.

For photons of 1.33 MeV, 15 cm of lead yields an attenuation of 99.995 percent and an energy absorption of 99.9 percent. With a detector collimator of this length containing a 2.5 mm $\times$ 5 mm slit, the maximum acceptance angle α is 2.1° along a

Table 3

Upper limits for the ratio of scattered to primary photons accepted by the detector collimator for selected tissue thicknesses

Tissue thickness (cm)	N_s/N	$[(N_s/N)f]$ (%)	Upper limit per cent scatter 0.1 f N_s/N (%)	Scatter angle ϕ	Fraction f of all scattered photons ($\times 10^2$)
10	0.90	0.27	0.03	0–6°	1.4153
15	1.61	0.43	0.04	0–5°	0.9866
20	2.60	0.70	0.07	0–4°	0.6328
25	3.95	1.07	0.11	0–3°	0.3559
30	5.82	1.57	0.16	0–2°	0.1575
35	8.39	2.26	0.23	0–1°	0.0386
40	11.94	3.23	0.32		

diagonal in the collimator slit. For a source collimator with a 2 mm × 4 mm slit positioned 50 cm from the source, the maximum divergence angle β is 0.51° along the slit diagonal. With this combination of collimators, the maximum scattering angle Φ is 2.6° for photons reaching the detector. From the Klein-Nishina equation, the fraction f of all ^{60}Co scattered photons confined to scattering angles from 0° to 2.6° is f = 0.0027. Under the good geometry conditions employed for transmission scanning, the ratio N_S/N of photons scattered in the patient to primary photons reaching the detector is:

$N_S = N_0 - N$ N_0 = number of primary photons reaching detector with no scattering medium present

but $N_0 = N\ EXP\ (\mu t)$

$N_S = N\ [EXP\ (\mu t) - 1]$

$N_S/N = EXP\ (\mu t) - 1$ N = number of primary photons reaching detector with scattering medium present

The product of N_S/N and f is an overestimate of the ratio of scattered to primary photons reaching the detector, because photons are scattered at an angle ϕ isotropically about the direction of primary photons, and only a few ($< 1/10$) of the scattered photons enter the solid angle subtended by the detector-collimator assembly. As upper limits for the ratio of scattered to primary photons reaching the detector, values of 0.1 f N_S/N are listed in Table 3 for selected tissue thicknesses. From these data, it is apparent that the collimator design described above will reduce scattered photons to a negligible level ($< 0.3\%$). This analysis has been confirmed experimentally by attenuation curves measured in water and lead for detector collimators with dimensions of 3 cm × 3 cm, 1 cm × 1 cm, 4 mm × 6 mm and 2 mm × 4 mm. For the smallest collimator slit, measured attenuation curves correspond closely to curves computed for a narrow beam of ^{60}Co photons.

With the source and detector arrangement described above, a minimum source

activity can be computed which will provide 10 000 detected photons (1 %, 1σ statistics) per measurement point with a maximum patient thickness of 40 cm between source and detector. For ^{60}Co photons, a cylindrical NaI crystal 10 cm thick provides an estimated detector efficiency $\varepsilon = 0.85$ in current mode. A detector collimator slit with dimensions of 2.5 mm × 5 mm has a cross-sectional area A = 0.125 cm^2. With these values and equation (5), the maximum photon flux density Φ at the detector is 19.6×10^6 photon/cm^2/s for L = 40 cm, T = 10 s, I = 0.25 cm and P = 0.077. This value of Φ corresponds to an exposure rate of 43.3 R/h at the detector with the patient absent. For a source-detector distance 1.5 meters, a lower limit (self-absorption in ^{60}Co source neglected) of 77 Ci may be estimated for the ^{60}Co source.

A most important consideration is the absorbed dose to a patient examined with the transmission scanning assembly. To estimate the patient dose, the absorbed dose distribution was computed for a single transmission scan of a patient with a 40 cm diameter circular cross section. These data were summed over k_{max} angular orientations of source and detector to obtain the absorbed dose distribution delivered during the entire examination. Data for the computation included a beam width of 0.5 cm, depth dose data for 0 cm × 0 cm field, a scanning time of 10 seconds at one angular orientation, and an exposure rate of 1 R/min at 80 cm from the ^{60}Co source. For 60 angular orientations of source and detector, the maximum dose delivered to a 40 cm thick circular patient is 0.084 rad; for 120 orientations, this value would double to 0.169 rad. The exposure rate computed above of 43.3 R/h at the detector corresponds to 2.54 R/min at the 80 cm distance from source to patient surface. Hence, the absorbed dose of 0.169 rad for 120 angular orientations and 0.25 cm spatial resolution should be increased by a factor of 2.54 to a maximum dose of 0.43 rad. For patients less than 40 cm thick, the maximum dose would be decreased significantly.

Image reconstruction

In an object exposed to a narrow parallel beam of monoenergetic photons, the transmitted intensity I_x (e.g. the photon flux density) is related to the incident intensity I_0 by the expression

$$I_x = I_0 \, \mathrm{EXP}\left[- \int_{-\infty}^{\infty} \mu(x, y) \, \varrho(x, y) \, dy \right] \tag{10}$$

where $\mu(x, y)$ is the mass attenuation coefficient distribution function of the object for the photons employed, and $\varrho(x, y)$ is a function describing the physical density distribution of the object. Equation 10 may be rewritten

$$\log I_0 - \log I_x = \int_{-\infty}^{\infty} \mu(x, y) \, \varrho(x, y) \, dy = \int_{-\infty}^{\infty} f(x, y) \, dy = g(x) \tag{11}$$

where f(x, y) is a general density function (specifically, f(x, y) is the linear attenuation coefficient) incorporating the mass attenuation coefficient and the physical

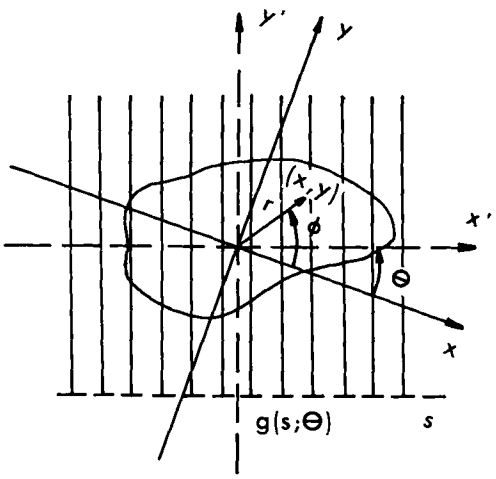

Fig. 4. Set of functions $g(s;\theta)$ describing the transmitted photon intensity at any location along a line parallel to the x′ axis.

density functions, and g(x) is a transmission function. If the object is scanned at several angles θ by rotating the coordinate axes, then a set of functions $g(s;\theta)$ is obtained which describes the transmitted intensity at any location s along a line parallel to the x′ axis below the object for any scan angle θ (Fig. 4).

By application of Fourier transform properties, f(x, y) may be reconstructed from transmission scan data $g(s;\theta)$. The Fourier transform of f(x, y) in cartesian coordinates is

$$F(X, Y) = \int_{-\infty}^{\infty}\int_{-\infty}^{\infty} f(x, y)\ \mathrm{EXP}\,[+2\pi i(xX + yY)]\,dxdy$$

and the inverse transform is

$$f(x, y) = \int_{-\infty}^{\infty}\int_{-\infty}^{\infty} F(X, Y)\ \mathrm{EXP}\,[-2\pi i(xX + yY)]\,dXdY \tag{12}$$

In polar coordinates

$$f(r, \phi) = \int_{0}^{2\pi}\int_{0}^{\infty} F(R, \theta)\ \mathrm{EXP}\,[-2\pi iRr\cos(\phi - \theta)]\,RdRd\theta \tag{13}$$

Through a series of manipulations, this equation may be expressed in terms of the transmission function $g(s;\theta)$ according to the two equations:

(a) The one-dimensional Fourier transform of $g(s;\theta)$ given by

$$F(R;\theta) = \int_{-\infty}^{\infty} g(s;\theta)\ \mathrm{EXP}\,(2\pi isR)\,ds$$

(b) The two-dimensional Fourier transform of the function $F(R, \theta)$ given by

$$f(r, \phi) = \int_0^{2\pi} \int_{-\infty}^{\infty} F(R, \theta)\, EXP\,[-2\pi iRr \cos(\phi - \theta)]\, RdRd\theta \tag{15}$$

By application of the convolution theorem (RAMACHANDRAN & LAKSHMINARAYANAN 1971), the Fourier transforms above may be reduced to two single discrete summations. The first is

$$g'(na; \theta) = a \sum_{m=-\infty}^{\infty} g(ma; \theta)\, q[(m-n)a] \tag{16}$$

where $g(ma; \theta)$ describes the transmission data at a set of equally spaced points $s = ma$, where m is a positive or negative integer and a is the spacing interval between points. In equation 16, the function $g(ma; \theta)$ is convolved with the expression $q[(m-n)a]$ to yield $g'(na; \theta)$, the convolved form of the transmission data. Since $q[(m-n)a]$ equals $1/4a^2$ for $(m-n) = 0$,

$$\frac{-1}{\pi^2(m-n)^2a^2} \text{ for } (m-n) \text{ odd, and zero for } (m-n) \text{ even,} \tag{17}$$

equation (16) may be rewritten

$$g'(na; \theta) = \frac{g(na; \theta)}{4a} - \frac{1}{a\pi^2} \sum_{p\ odd} \frac{g[(n+p)a; \theta]}{p^2} \tag{18}$$

where p now equals $(m-n)$. The second summation calculates $f(r, \phi)$ in the discrete form $f(jr_0, k\phi_0)$ by summing $g'(na; \theta)$ over θ as follows:

$$f(r, \phi) = f(jr_0, k\phi_0) = \theta_0 \sum_{k=1}^{k_{max}} g'[jr_0 \cos(t\phi_0 - k\theta_0), k\theta_0] \tag{19}$$

where j, k, k_{max} and t are integers, and r_0 and ϕ_0 are spacing intervals for r and ϕ. The spacing interval for θ is $\theta_0 = \pi/k_{max}$, where k_{max} is the number of transmission scans recorded at periodic intervals between $-\pi/2$ and $\pi/2$. Since the value of $jr_0 \cos(t_{\phi_0} - k_{\theta_0})$ is generally not a multiple of a, interpolation between computed values of $g'(na; \theta)$ is necessary. The resolution of the final data $f(r, \phi)$ is dependent upon the accuracy of this interpolation, and, consequently, upon the size of the spacing interval a for the transmission data.

Equations 18 and 19 are readily adaptable to computer analysis. Furthermore, these equations permit the reconstruction to take place in real space only, and a transformation to reciprocal space is not required.

The array I(M, k) consists of data describing the transmitted beam intensity for a finite number M_{max} of points separated by an interval a for each angle $k = 1$ to k_{max} at which transmission data are obtained. The positive integers M and k are suitable for use with a variety of programing languages. From equation 11, for an incident intensity I_0 the transmission function G(M, k) corresponding to $g(ma; \theta)$ may be expressed as

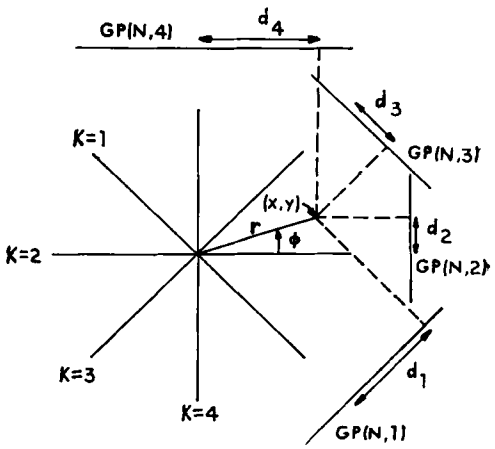

Fig. 5. The parallel beam scanning technique of the summation process described by equations 20, 21 and 22.

$$G(M, k) = \log I_0 - \log I(M, k). \tag{20}$$

The simplest form of the convolved transmission data GP(N, k) corresponding to $g'(na; \theta)$ is derived under conditions of a one-to-one correspondence for M and N (i.e. $M_{max} = N_{max}$). From equation 18,

$$GP(N, k) = \frac{G(N, k)}{4a} - \frac{1}{a\pi^2} \sum_{p\,odd} \frac{G[(N+P), k]}{p^2} \tag{21}$$

where p is limited to odd values, $-M_{max} \leq p \leq M_{max}$, for the finite case. To determine the general density function f(x, y) in rectangular coordinates (Fig. 5), values of r and ϕ are computed for each location (x, y), and f(x, y) is computed by an interpolative procedure for equation 22.

$$f(x, y) = f(r, \phi) = \theta_0 \sum_{k=1}^{k_{max}} GP(d_k, k) \tag{22}$$

where $d_k = r \cos(\phi - k\theta_0) + N_0$.

The point $M = N = N_0$ falls on a line passing through the origin and perpendicular to GP(M, k) and, therefore, I(M, k) and G(M, k). Since M and N are defined as sets of positive integers, the translation N_0 is necessary so that $d = N_0$ when $r = 0$. In general, integer values for d_k are not obtained (i.e., usually $N < d_k < N + 1$), and the projection of transmission scan data upon GP(N, k) for each point (x, y) must be determined by interpolation of $GP(d_k, k)$ between GP(N, k) and GP(N + 1, k).

To determine the correctness of this approach to two-dimensional image reconstruction, equations 20, 21, and 22 were evaluated for several simulated experiments utilizing computer generated, moving source and detector transmission data. These experiments are described below.

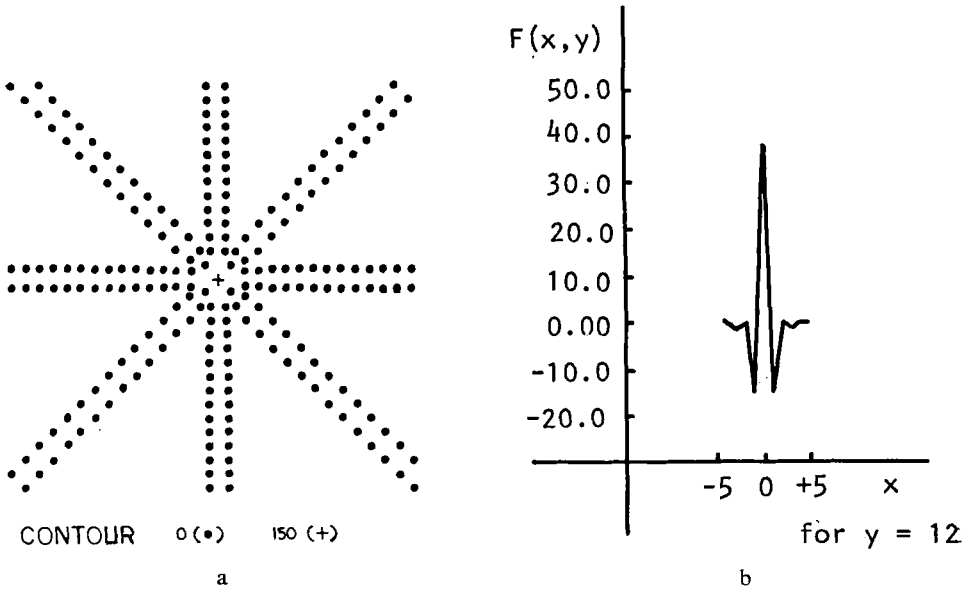

a b

Fig. 6. Image reconstruction for simulated transmission scan data generated by a delta function: a) zero contour plot for the point spread function resulting from the image reconstruction program; b) the function f(x, y) for a typical cross section away from the origin centered along a line through (0, 0) which represents one direction in which transmission data were obtained. The negative overshoot is a result of the Fourier transform process inherent in the convolution method. A plot GP(N,k) versus N has a similar shape and is related numerically by the multiplicative factor θ (equation 22).

Point spread function for the image reconstruction process. Transmission data generated with a delta function were submitted to the image reconstruction program. The resultant point spread function (PSF) was a characteristic two-dimensional star image (Fig. 6) not unlike those often encountered in data processing techniques for nuclear medicine images. The number of rays intersecting at the image center equals the number of angles for which simulated scan data were entered. The rays are symmetrical about the x − y axes and are spaced equally from each other, as were the transmission scans.

The integration in equations 10 and 11 can be interpreted as 'looking through' the delta-function at zero and summing the values of everything seen along the line of sight—in this case only the spike at (0, 0). Effectively then, GP(N, k) is not a one-dimensional but a two-dimensional function whose extension into the second dimension is shown in Fig. 7 a. By superimposing GP(N, k) extended planes at appropriate angles θ, the data ensemble shown in Fig. 7 b is obtained.

The radial rippling effect exhibited in Figs 6 a and 7 b accompanies the convolution process and decreases markedly with an increase in the number of orientations at which transmission data are obtained. That is, the radial rippling effect decreases with increasing k_{max} (decreasing θ_0); moreover, as $k_{max} \to \infty$, the ensemble of GP(N, k)

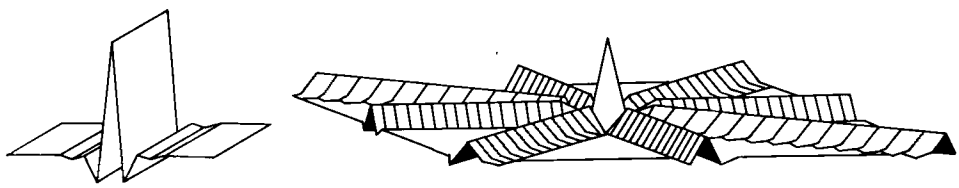

a b

Fig. 7. The two dimensional function GP(N, k): a) GP(N, k) along one angular orientation; b) GP(N, k) summed at appropriate angular orientations.

approaches a smoothly varying function with no periodicity and resembles a delta function surrounded by a zero plane of radius $r \to \infty$. Of course, to obtain a zero plane without variations, N must approach ∞ along with k_{max}. In the practical case, a generally satisfactory criterion relating the mean radius $\langle r \rangle$ of the scanned region, the sampling distance a for transmission data, and the equiangular interval θ_0 in radians is $\langle r \rangle \theta_0 \approx a$. As will be seen later, this criterion places rather severe restrictions on the image quality obtainable for a given combination of a, r, and θ_0.

Isoplanatic nature of the point spread function. The discussion above indicates that the PSF for parallel beam transmission scanning should be isoplanatic (i.e., the description of the function should be independent of the coordinates chosen for the center of the function). For an $x-y$ array of data describing the function for a selected value of k_{max} for central coordinates chosen at random, however, significant variations in the function are found when transmission data generation and image reconstruction programs are implemented. A few locations, in addition to the origin, selected for study of PSF's are shown in Fig. 8. These locations are A $(-5, 0)$, located on the x-axis at an integral multiple of the sampling interval $a = 1$ from the y-axis; B $(1, -1)$, located on a ray at an angle θ to the coordinate axes with x and y coordinates which are integral multiples of the sampling interval $a = 1$; and C $(-7, 5)$ and D $(3, 2)$ not located on rays but with x and y coordinates which are integral multiples of the sampling interval $a = 1$.

From digital printouts of the PSF at each location, an average of the PSF values along each ray through the spike center for a radius eight units or greater is given in Table 4. Sampling intervals of finite size for γ-ray transmission scans cause a loss of information for objects approximately the same size as the sampling interval. During the image reconstruction process, interpolation procedures cause additional information loss. These losses are illustrated in Table 4, where all values of the PSF should be 19 along rays 1–8 for all spike coordinates.

Specifically, the interpolation procedures affect the $GP(d_k, k)$ value determined between GP(N, k) and GP(N + 1, k). In Fig. 8 and Table 4, for example, point B lies directly on the ray $k = 2$, and a value of 19 is obtained for the function determined with this value for k. For $k = 6$, interpolative procedures are necessary for

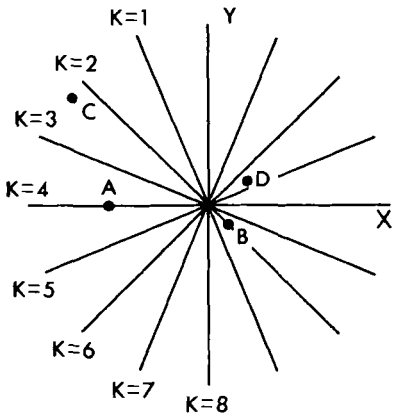

Fig. 8. Four locations (A, B, C and D) selected, in addition to the origin, for analysis of point spread functions for the moving source and detector scanning technique.

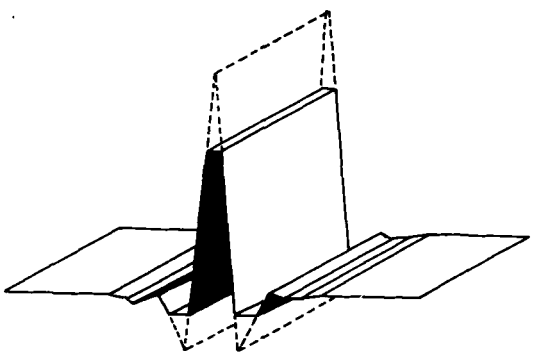

Fig. 9. Graphical display of the function GP(N, k) where the interpolation procedure has reduced the peak value of the function.

the function centered at B, since the perpendicular distance from the ray k = 6 through the origin to the point B is $\sqrt{2}$ rather than an integral multiple of a = 1, and the value of the function falls to 6. The result is a 'clipped' GP(N, k) function in the plane extended to two dimensions (compare Fig. 9 to Fig. 7 a). The values of the PSF are constant along rays k = 4 and k = 8 for all (x, y), because the spike coordinates are all integral multiples of the spacing interval a = 1. For the spike location (0, 0), all values for the function equal 19 for k = 1 to 8, because every ray (i.e., every value of k) intersects (0, 0), and no interpolation for the function is necessary.

If the sampling intervals for transmission scan data were much smaller than the

Table 4

Point spread function values for selected values of k, illustrating the apparent nonisoplanicity in the PSF introduced by discrete sampling intervals and interpolation procedures

Spike value at (x, y)	Coordinates of spike (x, y)	Approximate average value of PSF along ray k for k = 1 to 8 at a radius > 8 units								Sum of average PSF values for k = 1 to 8	Average value of PSF for all k	Ratio of average PSF to spike value
		k = 1	2	3	4	5	6	7	8			
154	(0, 0)	19	19	19	19	19	19	19	19	152	19.0	0.123
96	A (−5, 0)	8	6	16	19	16	6	8	19	98	12.3	0.128
92	B (1, −1)	6	19	6	19	10	6	19	19	95	11.9	0.129
89	C (−7, 5)	7	6	16	19	9	5	7	19	88	11.0	0.124
105	D (3, 2)	6	6	17	19	10	8	17	19	102	12.8	0.122

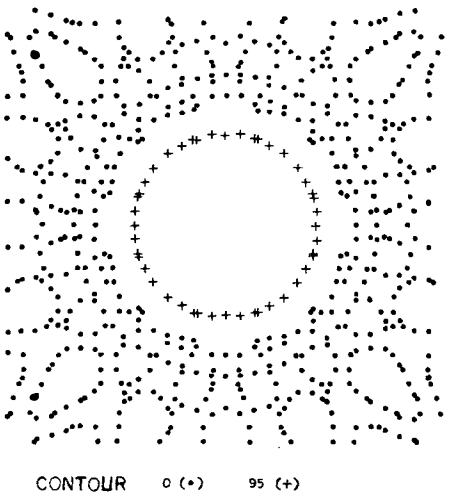

Fig. 10. Contour plot for circle centered at (0, 0), with $k_{max}=8$ and $\theta=\pi/8$. Scalloping outside the edge of the circle reflects a summation of the radial rippling effects depicted in Fig. 7 b.

interval a used for image reconstruction, then the interpolated value would reflect more accurately the actual value at d_k. Under these conditions, all PSF values in Table 4 would be much closer to 19, and the PSF would appear more isoplanatic.

The summation process described in Fig. 5 suggests that the sum of the average PSF values for each spike should be equal (within round-off error) to the maximum value of the spike. Also, the ratio of the average of all PSF values for all k to the spike value at (x, y) should be constant for all values of (x, y). These relationships are confirmed rather well in Table 4.

It may be concluded that the PSF is isoplanatic for the moving source, moving detector scanning technique, but that limitations accompanying use of discrete sampling intervals and interpolation procedures during image reconstruction furnish a PSF which appears nonisoplanatic. However, for an object much larger than the sampling interval, the PSF is isoplanatic even when discrete data sampling methods are used (see next section).

For the stationary source scanning technique, an analysis similar to that above reveals that, except for the point (0, 0), the radial arms of the PSF do not intersect at equiangular intervals, and the PSF is nonisoplanatic.

Image reconstruction process for a circle of uniform density. A contour plot is shown in Fig. 10 for a circle of uniform density and radius 7.5 (arbitrary units) centered at (0, 0) with $k_{max}=8$ and $\theta_0=\pi/8$. The scalloped configuration outside the circle boundary (identified by 95 isodensity contour) reflects a summation of the radial rippling effects depicted in Fig. 7 b, except that in Fig. 10 the summation is over the PSF for every point within the circle. Similar scalloping effects are displayed in Fig. 11 where $k_{max}=4$, $\theta=\pi/4$, and $r=5.0$ for circles centered at (0, 0) and (2, 4). Scalloping effects are symmetrical about multiples of θ_0, just as the radial rippling

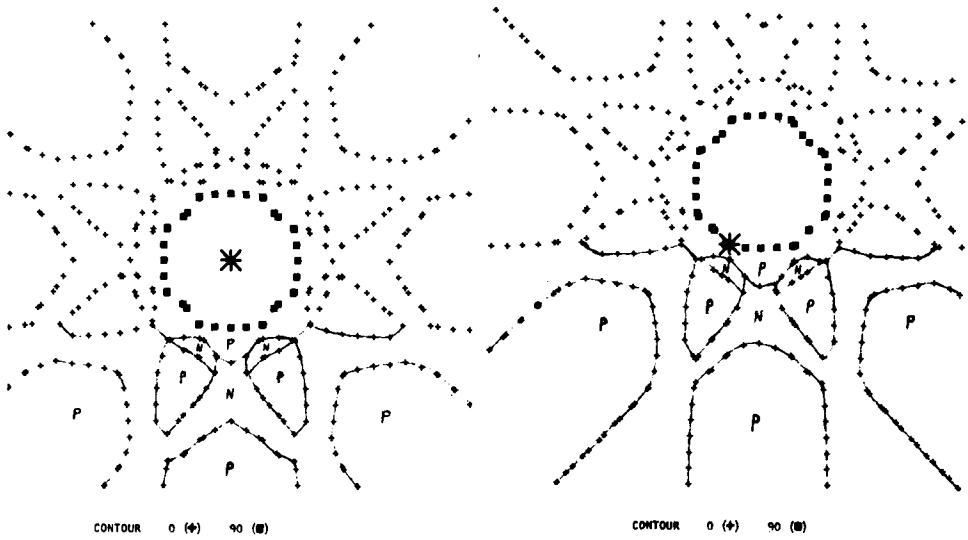

Fig. 11. Contour plot for circle of 5 units radius centered at (a) [(0, 0)] and (b) [(2, 4)], for $k_{max} = 4$ and $\theta_0 = \pi/4$. N and P indicate regions of negative and positive overshoot. Contours are 0(+) and 90 (■); the origin is denoted as (✳).

effect was symmetrical in Fig. 7 b for multiples of θ_0. Within the limitations of interpolation and plotting, the displays in Fig. 11 are identical, implying that the image reconstruction process does not introduce nonisoplanicity for data obtained by the moving source, moving detector scanning technique.

By closer adherence to the criterion

$$\langle r \rangle \theta \simeq a$$

the degree of scalloping can be greatly reduced. For the data in Figs 10 and 11, $\langle r \rangle = 10$ and $a = 1$, and the ideal value for θ_0 is 0.1 radian. However, in Fig. 10, $\theta = \pi/8 = 0.392$ radians, and in Fig. 11, $\theta_0 = \pi/4 = 0.785$ radians. These values are too large to provide unscalloped reconstruction images with adequate spatial resolution.

Image reconstruction process for three nonoverlapping circles each of uniform density. Transmission data were computed for circular objects of relative densities 50, 75 and 100 aligned as in Fig. 12 a. Reconstructed images of the objects displayed in Figs. 12 b–12 d demonstrate the influence of k_{max} upon the quality of the reconstructed image. The image in Fig. 12 d was obtained under conditions which satisfy the criterion $\langle r \rangle \theta \simeq a$, where $a = 1$ and $\langle r \rangle = 10$. The relative densities of the circles in the image 12D are estimated as 50, 75 and 100, corresponding to the densities of the original object. Image degradation increases as the approximation of $\langle r \rangle \theta$ to $a = 1$ decreases.

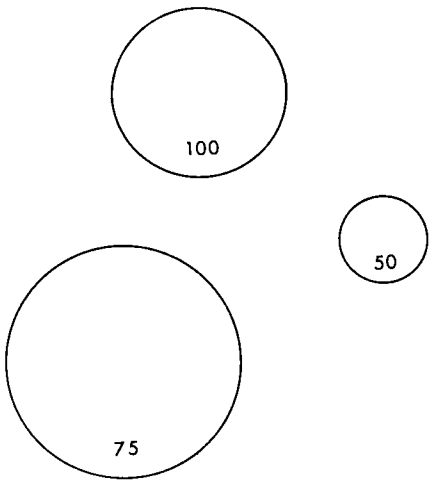

a

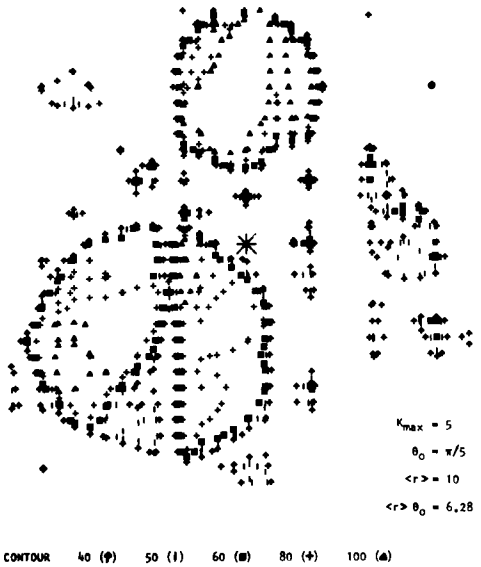

b

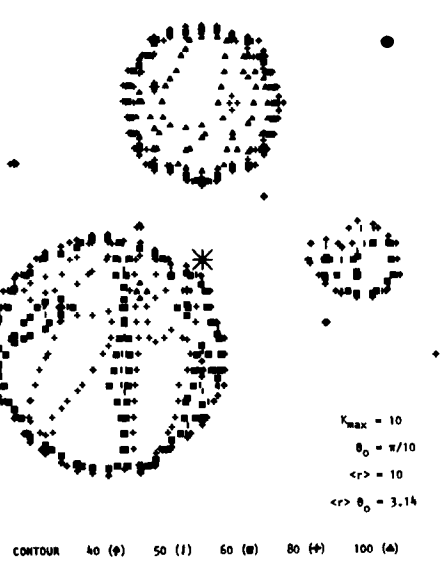

c

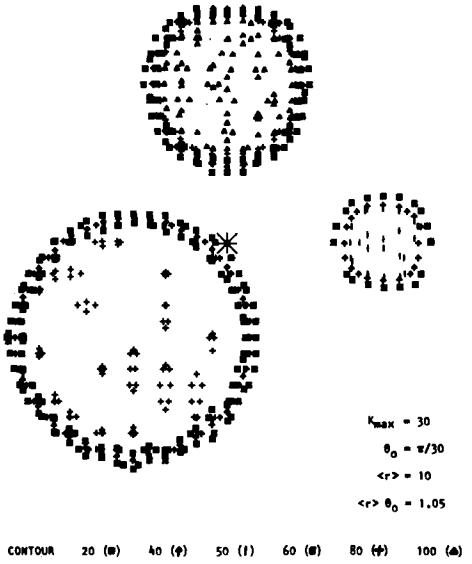

d

Fig. 12. Reconstructed images (b, c and d) for data depicted in (a), with increasing correspondence to the criterion $\langle r\rangle\theta_0 \cong a$. For (b), $k_{max} = 5$ and $\langle r\rangle\theta_0 \cong 6.28$. For (c), $k_{max} = 10$ and $\langle r\rangle\theta_0 \cong 3.14$. For (d), $k_{max} = 30$ and $\langle r\rangle\theta_0 \cong 1.05$.

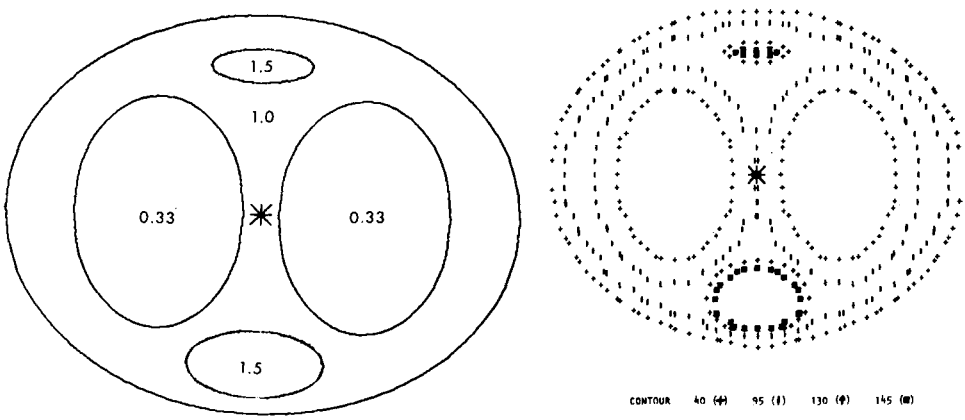

Fig. 13. a) Simulated human thoracic phantom, b) reconstructed image with $k_{max}=30$ ($\theta_0=\pi/30$). Contours are 40(+), 95(|), 130(†), and 145(■); the origin is denoted as (✳).

Image reconstruction process for objects simulating the human chest region. The thoracic cross section of a patient was approximated as an ellipse of unit density containing two ellipses of density 0.33 to represent lung, and two smaller ellipses of density 1.5 to represent the vertebral column and sternum (Fig. 13 a). Transmission data computed for the phantom with $k_{max}=30$ ($\theta=\pi/30$) were used to obtain the reconstructed image in Fig. 13 b. Slight distortions in the reconstructed image are a reflection primarily of interpolation inaccuracies. Some smoothing of boundaries is caused by finite sampling intervals. In the digital printout for the contour plot in Fig. 13 b, the density values average 0.334 for lung, 1.501 for bone and 1.000 for muscle, indicating good preservation of input density values during the image reconstruction process.

The reconstruction process as a clinical tool for determination of cross-sectional anatomy. Discussion of the image reconstruction process has been confined so far to convolution processes in the spatial domain. For these processes, either approach to γ-ray transmission scanning—moving source, moving detector, or stationary source, moving or stationary detector—may be used. The moving source and detector technique may be slightly superior because transmission measurements are independent of source-to-center-of-rotation and source-to-detector distances, and because the PSF is isoplanatic. Certain modifications to the γ-ray transmission procedure might reduce the data storage requirements for the image reconstruction process. Among these modifications are:

(1) Use of a circular or elliptical, rather than square, matrix for digital display of density values.

(2) Use of a logarithmic amplifier to express g(x) in equation 11 directly from input transmission scan data.

(3) Electronic convolution of the signal from a logarithmic amplifier to obtain GP(N, k) according to equation 21.

(4) Use of an analog-to-digital converter on the electronically processed signal, and storage of GP(N, k) directly on disc.

(5) Transferral of a transmission scan from disc to core, calculation of its contribution to each point in a circular array, and repetition of the process k_{max} times until the image is complete.

Although modifications such as those described above may improve the practicality of the image reconstruction process, a second problem may limit the clinical usefulness of cross-sectional anatomy reconstruction. This problem is the difficulty of obtaining at least 120 transmission scans of a patient in a reasonable length of time. Obviously, this time could be reduced by decreasing the number of transmission scans required for data accumulation and manipulation. The degradation of image quality accompanying a decrease in the number of transmission scans has been discussed, however, and this approach should not be contemplated unless a method can be identified to maintain image quality at an acceptable level. The approach discussed below—image deconvolution with a suitable PSF—appears capable of reducing the number of transmission scans with retention of acceptable image quality.

In the process of obtaining an image, an object 0 is distorted by the imaging system to furnish an image I (METZ 1969). The distortion introduced by the imaging system may be described by the function H characteristic of the system. The expressions O, H, and I in the spatial domain may be represented in the frequency domain by their respective Fourier transforms $0(\omega)$, $H(\omega)$ and $I(\omega)$.

$$0(\omega) \rightarrow H(\omega) \rightarrow I(\omega) \quad \text{where} \quad I(\omega) = 0(\omega)\,H(\omega) \tag{23}$$

That is, the image transform is the product of the object transform and the processing function transform. In transmission scanning, as in most imaging processes, the Fourier transform $I(\omega)$ can be computed from knowledge of the image I in the spatial domain, and the Fourier transform $H(\omega)$ of the processing system may be computed from physical measurements such as those yielding the point and line spread functions. Thus, the transform of the object may be obtained by the deconvolution process:

$$0(\omega) = \frac{I(\omega)}{H(\omega)} \tag{24}$$

The inverse transform of $0(\omega)$ then provides the original object 0:

$$0 = \mathfrak{F}^{-1}\,[0(\omega)] \tag{25}$$

The function H characteristic of the imaging system can be the point spread function (PSF), and the function $H(\omega)$ can be the Fourier transform of the PSF. In an

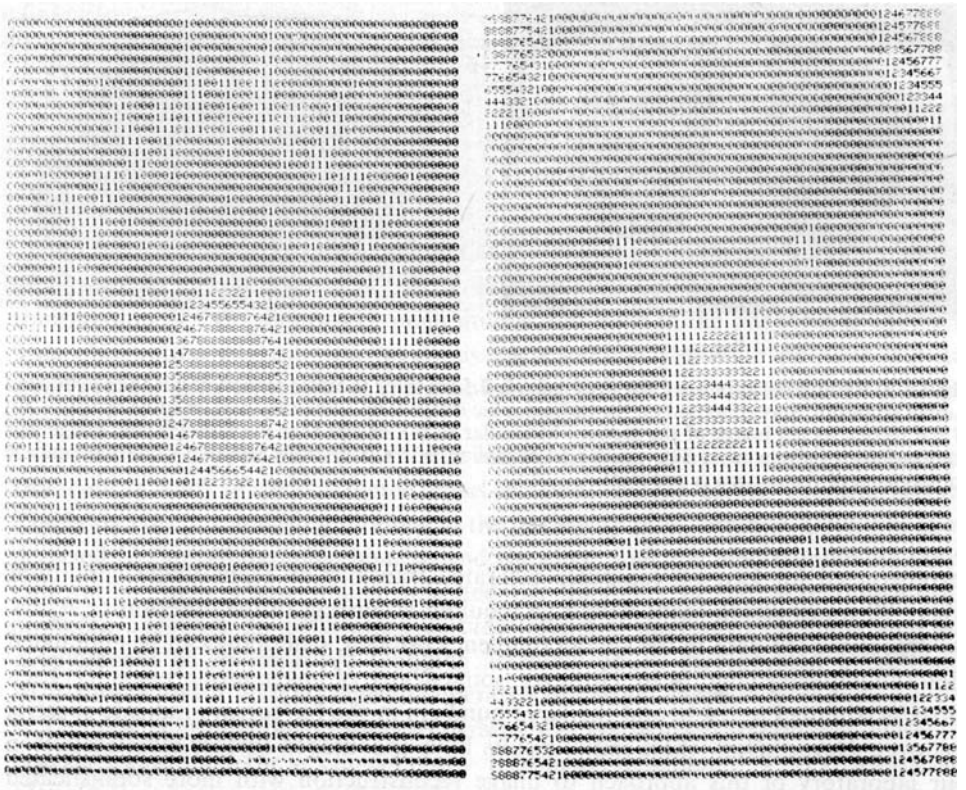

a b

Fig. 14. a) Image obtained with 8 computer generated transmission scans of a circular object, illustrating the severe scalloping which accompanies image processing in the spatial domain. The elliptical shape of the image is caused by the printout format. Density values are normalized to a maximum of nine. b) Image for same object as in (a), illustrating the suppression of scalloping obtained by processing the image in the spatial frequency domain. Spectral foldover is apparent in corners of the image. The elliptical shape of the image is caused by the printout format. Density values are normalized to a maximum of nine.

effort to identify the potential advantages of performing the image reconstruction process in the spatial frequency domain, a reconstructed image I of a circular object was transformed with a fast Fourier transform algorithm to obtain $I(\omega)$. With a single function $H(\omega)$ derived from the isoplanatic PSF, the image $I(\omega)$ was deconvolved with equation (24) to obtain $0(\omega)$. With equation 25, the object $0(\omega)$ then was transformed to the original object 0. This process illustrates the importance of PSF isoplanicity; if the PSF were not isoplanatic, a separate function $H(\omega)$ would be required for every point in the spatial frequency domain.

Rather unsophisticated applications of this approach to image reconstruction indicate that unscalloped images with satisfactory resolution may be obtained with considerably fewer transmission scans. The highly scalloped image in Fig. 14 a was

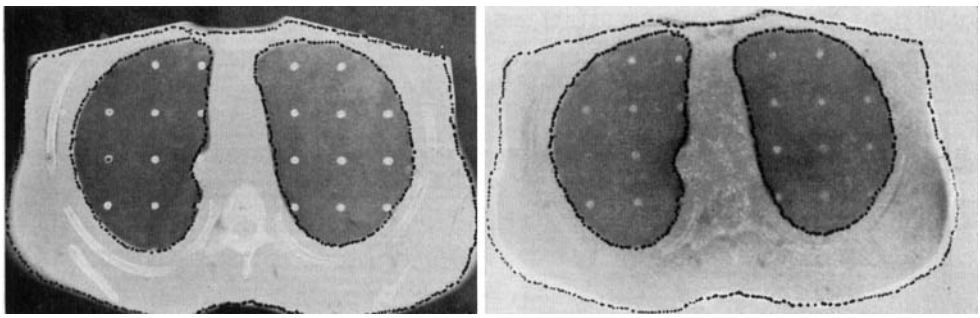

a b

Fig. 15. a) Radiographic image (50 kV) of a single 2.5 cm thick thoracic section of a Rando simulated human phantom. Superimposed on the radiographic image is an isodensity plot (relative density = 40) of the reconstructed image of the section. b) Similar to (a), except that the radiographic image was obtained with ^{60}Co γ rays. The similar transmission of ^{60}Co photons through bone and muscle components of the section is apparent.

reconstructed for $k_{max} = 8$ computer-generated transmission scans under conditions where 30 transmission scans would be required according to the criterion $\langle r \rangle \theta_0 \simeq a$. By processing the data in the spatial frequency domain, scalloping can be eliminated almost completely (Fig. 14 b). However, some degree of image unsharpness has been introduced into Fig. 14 b, and the large numbers in the far corners indicate spectral foldover. Nevertheless, these initial results have encouraged further investigation in our laboratory of this approach to image reconstruction with more sophisticated deconvolution techniques.

Experimental verification

Initial efforts towards reconstruction of cross-sectional anatomical images by γ-ray transmission scanning utilized a 2.5 cm thick thoracic section of a Rando simulated human phantom (Alderson Research Laboratories, Stamford, Conn.) and an elementary scanning apparatus consisting of a 10 mCi ^{60}Co source and a 2.5 cm × 2.5 cm NaI(Tl) detector. The detector was operated in pulse mode and was collimated by a lead cylinder 5.3 cm in length with a 5 mm × 15 mm slit. Transmission measurements equivalent to those obtained with the moving source, moving detector technique were achieved by aligning the source and detector in a stationary configuration and moving the thoracic section between the two. Angular orientations of the scanning assembly were simulated by manual rotation of the section.

The thoracic section had a mean radius $\langle r \rangle = 10$ cm, and, for a scan interval of 0.5 cm, transmission measurements at 60 angular orientations ($\theta_0 = 3°$) were required to satisfy the image reconstruction criterion. For each transmission measurement, at least 3 000 counts were accumulated to provide better than 2 percent counting statistics at the 1σ confidence level.

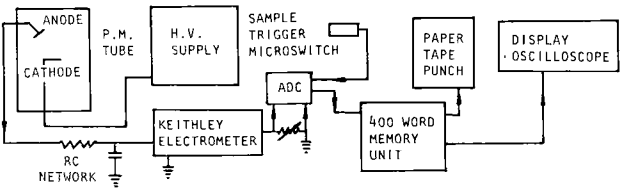

Fig. 16. Electronic assembly for γ-ray scanning.

Radiographic images in Fig. 15 a and 15 b were obtained by exposing the thoracic section to 50 kV roentgen and ^{60}Co γ rays, respectively. In Fig. 15 b, the similar transmission of ^{60}Co photons through muscle and bone in the phantom is apparent. This observation suggests that transmission scanning with ^{60}Co photons will not clearly reveal bony structures in the phantom, because these structures have a density near that of muscle.

Superimposed upon the radiographic images in Fig. 15 are isodensity plots (relative density = 40) of reconstructed cross-sectional images of the thoracic section. The body contour and lung outlines in the isodensity plots conform closely to those depicted in the radiographic images, and the chest wall and mediastinum are exhibited rather well. These results indicated the feasibility of the γ-ray transmission scanning approach to delineation of cross-sectional anatomy. The next step was development of an improved scanning assembly which incorporated a multicurie ^{60}Co source and a NaI(Tl) detector operated in current mode.

The new transmission scanning apparatus was constructed to conform closely to criteria established for a clinical γ-ray transmission scanner. A ^{60}Co teletherapy source was oriented with the beam directed horizontally at the detector collimator. A 15 cm long lead cylinder with a 2.5 mm $\times$ 5 mm slit served as the detector collimator. The source was collimated with four lead bricks (5 cm $\times$ 10 cm $\times$ 20 cm) forming a 2 mm $\times$ 4 mm slit at a distance of 50 cm from the source. Dimensions of the source-collimator slit provided a slight overlap of the ^{60}Co beam with the detector-collimator slit. To simplify mechanical construction, the source and detector remained stationary, and the phantom was mounted on a rotatable platform attached to the arm of a Picker Magnascanner. The scanner arm provided the linear motion of the phantom through the beam. The detector was a 2.5 cm $\times$ 2.5 cm NaI(Tl) crystal mounted permanently to a photomultiplier tube and surrounded by a lead housing for protection against scattered radiation. A negative high voltage (490 V) was applied to the cathode of the P.M. tube, and the anode current, after passing through a signal averaging RC network, was measured with a Keithley 610B electrometer (Fig. 16). A time constant of 0.047 seconds ($\sim$ 1/10 the sampling interval of 0.5 s) provided sufficient smoothing of the incoming signal and an adequate response to significant gradients in beam intensity. An analog-digital converter, on command of a microswitch attached to the scanning apparatus, sampled the output of the Keithley electrometer and produced a pulse train proportional to the input signal. A scaler in the 400 word memory unit counted the number of pulses in the train.

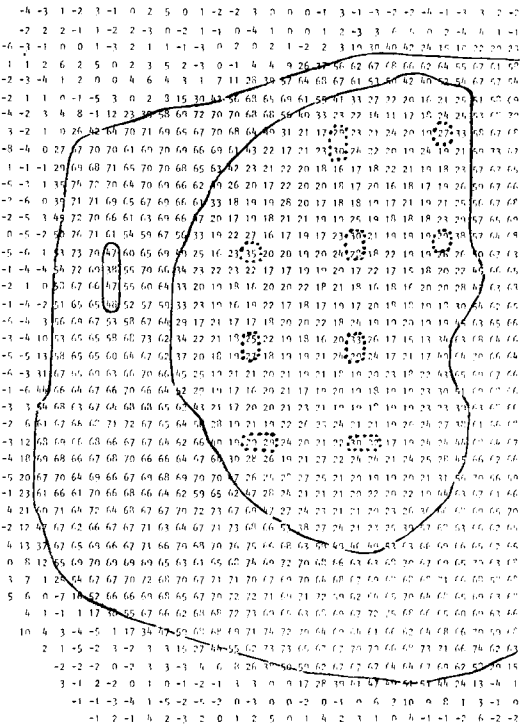

Fig. 17. Digital printout of relative densities in left part of thoracic section of simulated human phantom.

These numbers were stored in memory and, later, punched onto paper tape for delivery to the computer. As the phantom moved through the beam, the microswitch was activated by detents spaced at 0.5 or 0.25 cm intervals on a linear track.

Seven 2.5 cm thick slabs from the thoracic region of the Rando phantom were mounted on the scanner platform so that the photon beam traversed the center of the middle slab. Transmission of ^{60}Co photons was measured at 0.5 cm increments for $k_{max} = 60$ angular orientations ($\theta_0 = 3°$). By submitting the transmission data to the image reconstruction program, a density distribution was obtained for a cross section through the middle thoracic slab. The left portion of the printout is reproduced in Fig. 17. Division of the relative density values in Fig. 17 by 1 000 yields the linear attenuation coefficient (cm^{-1}) at each location. For ^{60}Co, this coefficient varies essentially only with the physical density (g/cm^3) and electron density (electrons/g) of the absorbing medium. Since biologic tissues have similar electron densities, the linear attenuation coefficients in Fig. 17 are a reasonable reflection of the physical density at each location. In Fig. 17, relative densities range from 60–68 for muscle and 16–24 for lung; divided by 1 000, these values agree well with the values of 0.064 cm^{-1} for muscle and 0.021 cm^{-1} for lung listed in Table 1.

When comparing structures in radiographic images to those outlined by isodensity

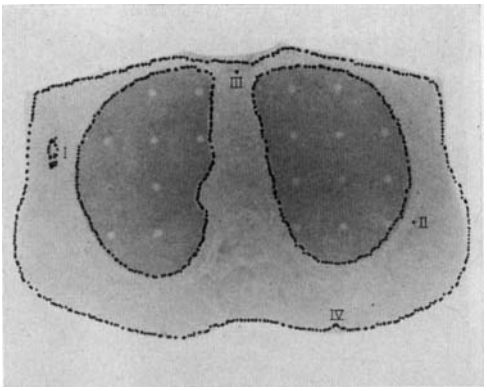

Fig. 18. Isodensity contours of 50 superimposed upon a radiographic image obtained with ^{60}Co γ rays.

contours or identified by inspection of digital density printouts, it is important to recognize that the reconstructed density distributions describe only those structures lying within the center 5 mm thickness of the phantom cross section, whereas the radiographic images depict the anatomy of the entire 2.5 cm thick slab. For example, this distinction helps to explain the slight displacement of the reconstructed image in Fig. 18 from the outer boundary of the slab depicted in the radiographic image. The displacement is a reflection primarily of the beveled outer surface of the phantom.

In Fig. 18, a number of structures, including the body and lung contours, are well defined by the 50 isodensity contour plot. In the upper left corner of the image, a rib contains a low density artefact (I) which extends into the 5 mm scanning section. A low density area (II) appears also inside the rib in the lower right corner of Fig. 18. Relative density values for these regions in the digital printout are reduced to just above 50, compared to muscle values of 60–68. The density value of 50 at (III) is caused probably by incomplete impregnation of the sternum with tissue equivalent plastic. The indentation of the body contour at (IV) is caused by a low density artefact confirmed by numerical values in the digital printout.

The Mix-D plugs (approximately 5 mm diameter) used to fill dosimeter voids in the phantom are significantly more dense than surrounding lung tissue, and are identified easily in the radiographic image in Fig. 18. Inspection of the digital printout (Fig. 17) distinctly reveals all plug locations in the lungs, because corresponding density values are significantly larger than density values for lung. The digital printout for Fig. 15 does not reveal the presence of the plugs, confirming the greater spatial resolution achieved with improved scanning and collimation techniques.

Seven sections of the head of the Rando phantom were mounted on the scanning platform so that the ^{60}Co beam scanned across a 0.5 cm thick cross section through the center slab of the phantom. The center of the scanned region was 0.75 cm above the base of the slab, and included as major structures the nose, ears, nasopharynx, teeth, and upper extensions of the mandible. In the radiographic images, the base of the skull is prominent in the 50 kV roentgenogram (Fig. 19 a) but only vaguely

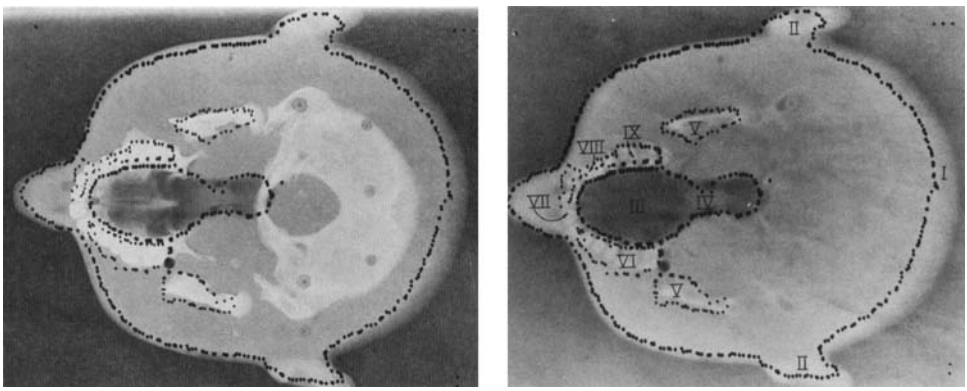

a b

Fig. 19. Isodensity contours superimposed upon (a) 50 kV roentgenogram and (b) ^{60}Co γ ray radiographic images for $k_{max} = 60$ transmission scans at 0.5 cm intervals. The middle of the 5 mm thick scanned region lies 0.75 cm above the base of this slab of the Rando phantom.

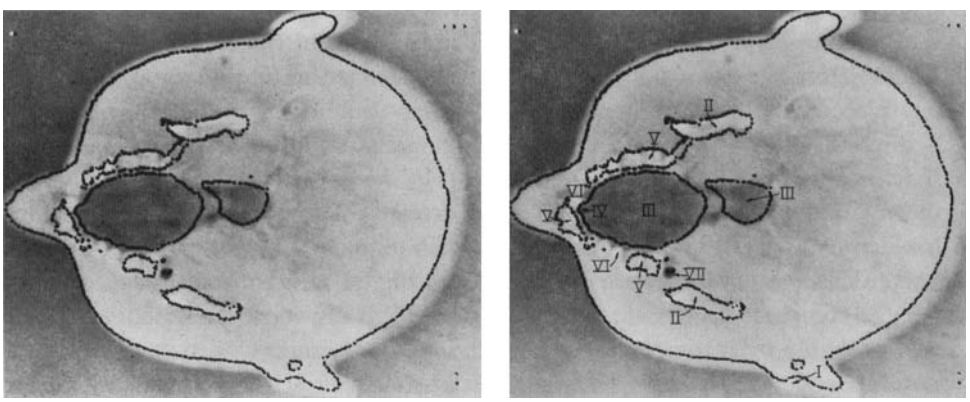

a b

Fig. 20. Isodensity contours superimposed upon a ^{60}Co γ ray image for $k_{max} = 90$ transmission scans at 0.25 cm intervals. The middle of the 5 mm thick scanned region lies 1.25 cm above the base of this slab of the Rando phantom.

distinguishable in the ^{60}Co image (Fig. 19 b). Hence, an image of the phantom skull cannot be expected with ^{60}Co transmission scanning. The ^{60}Co image suggests that structures which will be imaged most satisfactorily include the mandible, teeth, and nasopharynx, together with the outer contour of the head. Transmission data were accumulated for $k_{max} = 60$ angular orientations ($\theta_0 = 3°$) at 0.5 cm scan increments. The relative density contour 40 outlines the facial contour, ears, back of the head, and nasopharynx. The beveled edge of the back of the head interferes with correlation of the reconstructed contour and the radiographic image in this region. Inspec-

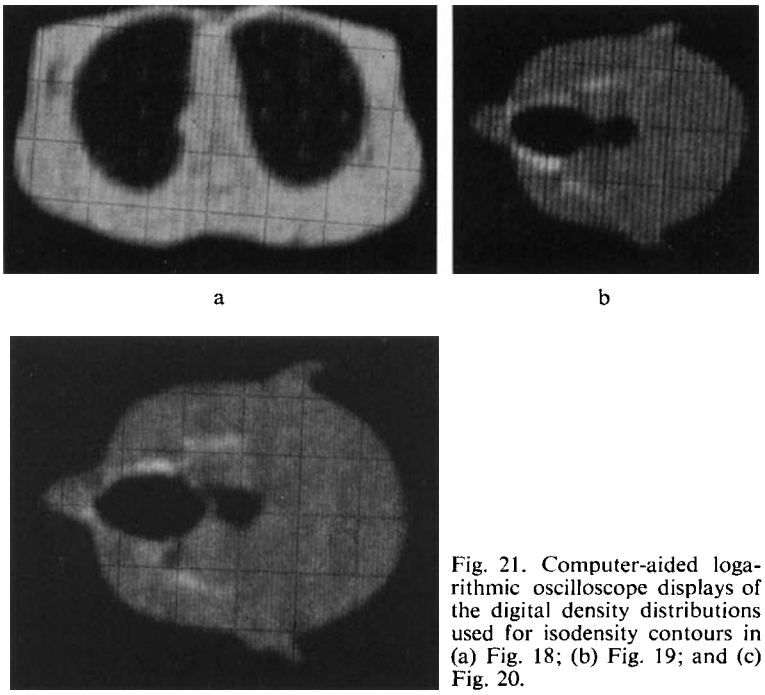

a b c

Fig. 21. Computer-aided logarithmic oscilloscope displays of the digital density distributions used for isodensity contours in (a) Fig. 18; (b) Fig. 19; and (c) Fig. 20.

tion of the phantom indicates that the reconstructed contour (I) should be inset approximately 0.75 cm from the blurred image of the back of the head. Both ear lobes were intersected by the ^{60}Co beam, and no indentation of the contour is apparent at the ears (II). The nasopharynx density values range from -2 to 6, corresponding to expected values near zero for an air cavity. The cavity at (III) is enclosed by an isodensity contour of 40. The constriction at (IV) reflects the presence of a septum slightly above the 0.75 cm scanning height. The mandible bones (V) exhibit density values of 84–96 and are fairly well defined by the 76 isodensity contour. Muscle density values range from 60 to 68. The scanning plane traverses the most dense parts of the teeth (VI), with density values from 100 to 120. The front teeth (VII) are imaged incompletely, probably because the phantom is asymmetrical in this region. The scanning plane slices the roots of the teeth at (VIII) and the back molars at (IX), and provides density values of 80–86.

To compare image resolution for transmission data obtained at scanning increments of 0.5 and 0.25 cm, transmission data for the phantom slab imaged in Fig. 19 were accumulated at 0.25 cm scan intervals for 90 angular orientations. An alignment discrepancy caused the center of the scanned region to be positioned at a height of 1.25 cm above the base of the slab (i.e., 0.5 cm above the region scanned for Fig. 19). A ^{60}Co image with superimposed relative density contours of 40 and 76

is shown in Fig. 20. At a height of 1.25 cm, the scanning plane traverses an indentation in one ear (I), and the 40 isodensity contour reveals this indentation. The mandible at (II) is better defined in the 0.25 cm scan image. The nasopharynx (two cavities at this height) is well defined. The protrusion of the cavity at (IV) has been confirmed in the phantom as a hole in the front of the palate. The high density areas (V) superimposed upon the teeth are, at this height, regions where the image plane intersects the hard palate just above the teeth. The palate is nonuniform, and the lower density areas (VI) above the teeth correspond to regions where the ^{60}Co beam passes through the roots of the teeth. For the missing Mix-D plug at (VII), density values of 38, much lower than muscle values of approximately 60, indicate that the 4 mm airfilled hole is just resolved.

With the aid of a small laboratory computer, the digital density distributions used for Figs 18 to 20 were displayed logarithmically on an oscilloscope screen. These displays (Fig. 21) provide considerably more information than plotted isodensity contours, and suggest that a display technique of this type may be preferred.

Conclusion

The feasibility of the transmission scanning approach to delineation of patient cross-sectional anatomy has been confirmed. Spatial resolution is limited primarily by scanner design considerations such as collimation, and by data handling and storage capabilities and the time available for data accumulation. The data accumulation time can be reduced (e.g., below the 30 minutes assumed for certain computations in the text) by using a source with higher photon flux density, replacing the single detector with a detector array, and employing selected data processing techniques. By redesign of the source collimator and the employment of multiple detectors, cross-sectional images for different planes could be obtained simultaneously.

The potential usefulness in radiation therapy treatment planning of the transmission scanning approach to delineation of cross-sectional anatomy is apparent. Extensions of the technique to medical diagnosis, facilitated by substitution of lower-energy photons for the ^{60}Co γ rays employed here, appear potentially rewarding. For control of resolution loss caused by patient motion, the collection of data in synchrony with predictable motion such as the respiratory cycle is being investigated. With the technique described here, a constant diameter water path is not needed around the anatomic region to be imaged. The technique is applicable to all regions of the body, and can be extended to higher resolution investigations of limited anatomic regions.

SUMMARY

^{60}Co γ-ray transmission data were measured along linear scan paths at a number of angular orientations with respect to the patient and submitted to a computer software program. Reconstructed images are displayed as digital density printouts and as isodensity

contours on an x – y plotter or oscilloscope screen. Image resolution is limited primarily by factors such as collimation and the amount of transmission data collected; with the rather rudimentary apparatus at disposal, a spatial resolution better than 5 mm has been achieved.

ZUSAMMENFASSUNG

Die ^{60}Co Gammastrahlen Transmissions-Werte längs linearer Scan-Wege wurden bei einer Anzahl von Winkelorientierungen gegenüber dem Patienten gemessen und mit Hilfe eines Komputerprogramms bearbeitet. Die rekonstruierten Bilder wurden als digitale Dichtezifferwerte und als Iso-Dichte Konturen mit einem x–y Schreiber oder auf einem Oscilloskopschirm dargestellt. Die Bildauflösung ist primär durch Faktoren wie die Kollimation und die Menge der gesammelten Transmissionswerte begrenzt; mit der für die vorliegende Untersuchung ziemlich rudimentären Ausrüstung wurde eine räumliche Auflösung von weniger als 5 mm erreicht.

RÉSUMÉ

Les auteurs ont mesuré la transmission du rayonnement gamma du ^{60}Co le long de balayage linéaire fait suivant différentes orientations angulaires par rapport au malade et ils ont soumis ces résultats à un programme d'ordinateur. Les images reconstruites sont représentées par des clichés indiquant la densité digitale et par des contours d'isodensité sur un traceur x–y ou sur un écran d'oscilloscope. La résolution de l'image est limitée à la base par des facteurs tels que la collimation et la quantité des mesures de transmission enregistrées. Cet appareil plutôt rudimentaire a donné une résolution spatiale supérieure à 5 mm.

REFERENCES

BERGER M. and DOGGETT J.: Response function of NaI(Tl) scintillation counters. Rev. Sci. Inst. 27 (1956), 269.

CORMACK A.: Reconstruction of densities from their projections, with applications in radiological physics. Phys. in Med. Biol. 18 (1973), 195.

— Representation of a function by its line integrals, with some radiological applications. II. J. appl. Phys. 35 (1964), 2908.

FARMER F. and COLLINS M.: A new approach to the determination of anatomical cross-sections of the body by Compton scattering of gammarays. Phys. in Med. Biol. 16 (1971), 577.

GILBERT P.: Iterative methods for the three-dimensional reconstruction of an object from projections. J. theoret. Biol. 36 (1972), 105.

GOITIEN M.: Lawrence Radiation Laboratory Report, LBL 547 (1971).

GORDON R., BENDER R. and HERMAN G.: Algebraic reconstruction techniques (ART) for three-dimensional electron microscopy and x-ray photography. J. theoret. Biol. 29 (1970), 471.

IBBOTT G. and HENDEE W.: Unpublished data.

JOHNS H. and CUNNINGHAM J.: The physics of radiology. Third edition, p. 746. Charles C. Thomas, Springfield, Illinois 1970.

KAISER W.: Scintillation spectrometry. The state of the art. Anal. Chem. 38 (1966), 28.

KUHL D. and EDWARDS R.: The Mark III scanner. A compact device for multiple-view and section scanning of the brain. Radiology 96 (1970), 563.

METZ C.: A mathematical investigation of radioisotope scan image processing. Ph. D. thesis, University of Pennsylvania, 1969.

RADON J.: Über die Bestimmung von Funktionen durch ihre Integralwerte längs gewisser Mannigfaltigkeiten. Ber. Verh. Sachs. Akad. Wiss. 69 (1917), 262.

RAMACHANDRAN G. and LAKSHMINARAYANAN A.: Three-dimensional reconstruction from radiographs and electron micrographs: application of convolutions instead of Fourier transforms. Proceedings of the National Academy of Sciences, USA, Vol. 68, No. 9, September, 1971.

SMITH P., PETERS T. and BATES R.: Image reconstruction from finite numbers of projections. J. Phys. A.: Math., Nucl. Gen. 6 (1973), 361.